Journal of Alloys and Compounds 990 (2024) 174459

Contents lists available at ScienceDirect

Journal of Alloys and Compounds

journal homepage: www.elsevier.com/locate/jalcom

# Microstructural evolution and mechanical behavior of novel $TiZrTa_xNbMo$ refractory high-entropy alloys

Xiangyang Shen [a], Zihe Guo [a], Feng Liu [a], Fuyu Dong [a,*], Yue Zhang [a,*], Chao Liu [a], Binbin Wang [b], Liangshun Luo [b], Yanqing Su [b], Jun Cheng [c,*], Xiaoguang Yuan [a], Peter K. Liaw [d]

[a] School of Materials Science and Engineering, Shenyang University of Technology, Shenyang, China
[b] School of Materials Science and Engineering, Harbin Institute of Technology, Harbin, China
[c] Northwest Institute for Nonferrous Metal Research, Shaanxi Key Laboratory of Biomedical Metal Materials, Xi'an 710016, China
[d] The Department of Materials Science and Engineering, University of Tennessee, Knoxville, TN, USA

ARTICLE INFO

*Keywords:*
Refractory high-entropy alloy
Phase-diagram calculation
Elemental segregation
Strength-plasticity relationship
Solid-solution strengthening

ABSTRACT

The refractory high-entropy alloy (RHEA) with a body-centered-cubic (BCC) solid-solution structure has excellent high-temperature softening resistance, which has attracted wide interest in the field of high-temperature alloys. However, its limited room-temperature plasticity has greatly hindered its engineering application. To obtain an excellent strength-plasticity matching relationship, in this reported study, the Ta content in the high-entropy alloy (HEA) was adjusted to rectify this shortcoming. A series of $TiZrTa_xNbMo$ (x = 1.0, 0.9, 0.8, 0.7, and 0.6 at. percent, at%) RHEAs were prepared using the vacuum arc-melting technique, and the microstructure and mechanical properties of these RHEA alloys were systematically investigated. The experimental results show that the $TiZrTa_xNbMo$ RHEAs are composed of main BCC1 and minor BCC2 phases, which exhibit a dendritic structure. By reducing the Ta content, the elemental segregation caused by the non-equilibrium solidification is reduced. In terms of mechanical properties, with the decrease of Ta content, the hardness and room-temperature yield strength of the alloy decreases slightly, but the room-temperature plasticity increases significantly. The Ta0.7 alloy has the highest plasticity (34.8 %), which is about twice that of the equimolar Ta 1.0 alloy, while the yield strength remained at 1297 MPa. The excellent mechanical properties of the alloys can be attributed to solid-solution strengthening and the formation of moderate amounts of interdendritic regions. The interaction between slip bands and dislocations formed during compression of the Ta0.7 alloy decreased its work hardening. Moreover, the theoretical model of solid-solution strengthening elucidates that the calculated values of the alloy's yield strength are consistent with that obtained experimentally.

## 1. Introduction

As the economic progress of developed nations continues to stretch the limits of science and technology, traditional metal alloys consisting of one or two main elements can no longer meet the increasing service demands of metals. To overcome this challenge, in 2004, Yeh et al. proposed a new concept of the high-entropy alloy (HEA), which consists of solid-solution alloys composed of five or more elements in equimolar or near-equimolar proportions [1–3]. The proposal of the HEA strategy broke the design concept of traditional alloys and became an important milestone in the development history of metal materials. Due to the high-entropy effect, lattice distortion, slow diffusion, and cocktail effect, HEAs exhibit outstanding properties, such as high strength, great toughness, strong wear resistance, and radiation resistance [4–9]. Consequently, substantial research is now being devoted to the development of these novel alloys, including concept verification, alloy design, advanced manufacturing, and advanced characterization. It is hoped that a new type of metal material with excellent performance and function can be obtained, to overcome harsh environmental conditions. RHEAs composed of high melting point elements (Ti, Zr, Hf, Nb, Ta, and Mo) have attracted wide attention due to their excellent high-temperature mechanical properties. For example, WTaNbMo and WTaNbMoV alloys with a BCC structure were successfully prepared for the first time by Senkov et al. [10]. These alloys were found to have compressive yield strengths of 477 MPa and 405 MPa at 1600 °C [11].

Recently, as more RHEAs have been successfully developed, the field

* Corresponding authors.
*E-mail addresses:* dongfuyu2002@163.com (F. Dong), yuezhang@sut.edu.cn (Y. Zhang), 524161386@qq.com (J. Cheng).

https://doi.org/10.1016/j.jallcom.2024.174459
Received 25 September 2023; Received in revised form 6 April 2024; Accepted 8 April 2024
Available online 9 April 2024

of biomedicine has become a current research hotspot. As a member of the RHEA alloy system, TiNbTaZrMo RHEA has great potential to become a new generation of biomaterials [12–15]. Compared with traditional biomaterials, TiNbTaZrMo RHEA has several advantages. The BCC solid solution structure endows the TiNbTaZrMo RHEA with high hardness, high strength and good wear resistance, which avoids the disease caused by human joint wear. In addition, although some medical Ti and Ti based alloys have good biocompatibility, their poor wear resistance makes them unsuitable for artificial joint support. From the perspective of safety and health, Ti, Nb, Ta, Zr and Mo are non-toxic and allergic-free elements, and have good corrosion resistance, which will not cause damage to the human body. Therefore, TiNbTaZrMo RHEA is a promising material. However, the low ambient-temperature plasticity of this alloy seriously hinders its further practical application. It is well known that adjusting the alloy's component content is an effective method for modifying the mechanical properties of alloys [16–20]. For HEAs, on the one hand, the required properties can be obtained by simultaneously changing the content of multiple components in the alloy. For example, Hori et al. [21] developed a series of non-equiatomic Ti-Nb-Ta-Zr-Mo HEAs, such as $Ti_{0.6}Zr_{0.6}Nb_{1.4}Ta_{1.4}Mo_{1.4}$, $Ti_{1.4}Zr_{1.4}Nb_{0.6}Ta_{0.6}Mo_{0.6}$, and $Ti_{1.7}NbTaZrMo_{0.3}$, which had better mechanical properties than the equimolar TiNbTaZrMo RHEA. On the other hand, the properties of the alloy can also be optimized by modifying the content of one component. In this case, Hua et al. [15] studied the effect of Ti addition on the $Ti_xNbTaZrMo$ HERA and found that an increase in the Ti content caused a gradual decrease in the alloy's the yield strength. However, it was also noted that this step yielded the alloy's plasticity to initially decrease and then increase. Wang et al. [22] demonstrated that the addition of Mo can significantly increase the hardness and yield strength of a $TiNbTaZrMo_x$ RHEA, while weakening the alloy's room-temperature plasticity.

Tantalum is one of the elements that is routinely added to refractory alloys, because of its high melting point, strong corrosion resistance, high chemical stability, and small expansion coefficient. As such, it is widely used in the preparation of evaporators, electronic components, and jet engines [23–28]. In addition, due to tantalum's large atomic radius, its addition can cause strong lattice distortions in a HEA, thereby enhancing the solid-solution strengthening effect. However, previously reported studies have shown that the element with the highest melting point in an RHEA is usually one of the reasons for the room temperature brittleness [29]. Therefore, for the TiZrTaNbMo RHEA, the strategy of reducing the content of Ta element with the highest melting temperature in the alloy system was adopted, in an attempt to greatly improve the plasticity of the alloy without significantly reducing the yield strength. Furthermore, the density of Ta (16.6 g/cm$^3$) is much higher than the other four elements in the alloy. So, reducing the Ta content can also reduce the overall density of the alloy, which is in line with the current trend of lightweight-alloy design.

In this reported study, based on the equimolar ratio of the TiZrTaNbMo RHEA, the microstructure and mechanical properties of a $TiZrTa_xNbMo$ RHEA were systematically investigated as the content of Ta was decreased. The formation of a solid solution, composition segregation, and the strengthening mechanism of the alloys were analyzed and discussed. It is hoped that the present work may play a guiding role in the optimization of the composition of HEAs, resulting in their subsequent engineering applications.

## 2. Experimental procedures

### 2.1. Composition design

Previous studies have shown that equimolar TaZrTiNbMo alloys are composed of dual BCC phase [14]. Nagase et al. [30] found that the formation of the dual-phase may be caused by the miscibility gap between Ta-Zr, Nb-Zr and Ti-Mo. Among them, Ta is the highest melting point element in the component, and its content obviously determines the distribution of one of the phases. In addition, as a promising metallic biomaterials, the density of TaZrTiNbMo RHEA is also crucial for its application prospects. Therefore, in this work, we selected to reduce the content of Ta element. The method of Calculation of Phase diagrams (CALPHAD) is a vital tool in the design and optimization of alloy compositions. Therefore, the pseudo-binary phase diagram of TiZrNbMo-Ta was calculated using the Thermo-Calc software (TCNI-5 database), as shown in Fig. 1. It can be seen from the figure that below the red dotted line, the dual-phase region decreases with the decrease of Ta content. Studies have shown that, reducing the thermodynamic miscibility gap between the composition is beneficial to the room temperature plasticity of the alloy [30]. At the same time, considering that the room temperature strength of the alloy should not be greatly reduced, the mole fractions of Ta were set to 0.2, 0.18, 0.17, 0.15, and 0.13, corresponding to Ta1.0, Ta0.9, Ta0.8, Ta0.7, and Ta0.6, respectively.

### 2.2. Alloy preparation and characterization

A series of $TiZrTa_xNbMo$ (x = 1.0, 0.9, 0.8, 0.7, and 0.6 at%) RHEAs, denoted as Ta1.0, Ta0.9, Ta0.8, Ta0.7, and Ta0.6, were prepared using a non-consumable vacuum arc furnace. In order to minimize the influence of impurity elements such as C, Si and O on the microstructure and properties of the alloy and ensure the accuracy of the sample composition, the purity of raw materials provided by the Beijing Dream Material Technology Co., Ltd are greater than 99.9 wt percent (wt%). The vacuum in the furnace was reduced to $\sim 5\times10^{-4}$ Pa, and then filled with argon (purity $\geq$ 99.999 %) for protection. Before melting, the residual oxygen in the furnace cavity was absorbed by the molten titanium. The mass of each button ingot was about 30 g. Due to the large difference in melting point and density of each component element, the alloy is difficult to be uniform during the smelting process. Therefore, in order to ensure the uniformity of the chemical composition, the raw materials are put into the copper mold of the electric arc furnace according to the melting point. Ti with the lowest melting point and Ta with the highest melting point are placed at the bottom and top of the copper mold, respectively. This avoids the difference between the actual composition and the theoretical composition caused by the volatilization of low melting point elements at high temperatures. The melting current was adjusted to ~300 A to fully melt the metal. Each button ingot was flipped and remelted 5 times. The button ingot gradually solidified in a copper mold with a diameter of 25 mm. In order to avoid oxidation during subsequent processing, the button ingots were placed in a quartz tube filled with argon and annealed at 1000 °C for 6 h. After heating, the

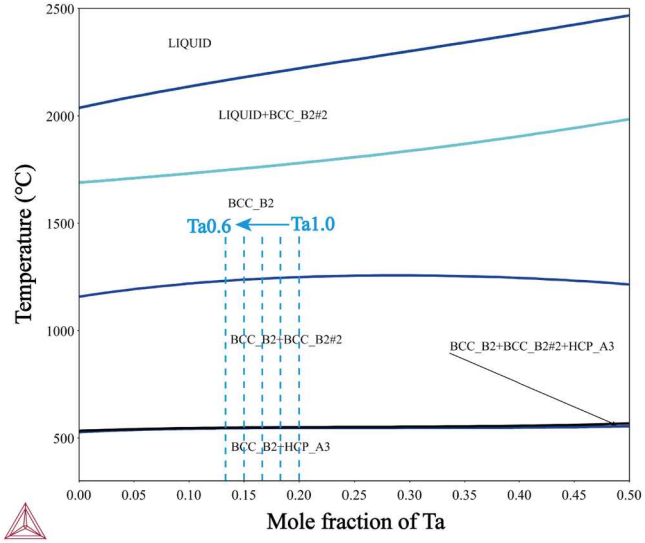


**Fig. 1.** Pseudo-binary phase diagram of TiZrNbMo-Ta.

samples were cooled in water. The size of the samples to be tested was obtained by wire-cut electrical discharge machining.

The crystal structures of the samples were revealed, using an X-ray diffractometer (XRD-7000, Shimadzu) employing Cu-Kα radiation in a 2θ range from 20 to 100°. The microstructure of the samples was observed by scanning electron microscopy (SEM, FEI Q45) and transmission electron microscopy (TEM, FEI Tecnai G2 F20). For the SEM analysis, the samples were first mechanically polished to the mirror surface, then etched in a 75 vol percent (vol%) HCl and 25 vol% $HNO_3$ solution for 4 min. For the TEM analysis, the samples were first polished with SiC paper to a thickness of ~ 50 μm and then thinned using an ion-polishing system (Gatan 691).

The density of the alloys was measured by the Archimedes method, and the average value of each sample was calculated after five measurements. The microhardness of the RHEAs was measured, using a Vickers hardness tester (UH250) under 9.8 N for 15 s. Ten data were collected in different parts of the sample, and the average value of these data was assigned as the sample's hardness. The room- temperature compression test was conducted with dimensions of Φ3×6 mm cylinder specimens using an electronic universal mechanical testing machine at an initial strain rate of $5 \times 10^{-4}$ $s^{-1}$. In order to ensure repeatability, three samples were prepared for the compression tests.

## 3. Results

### 3.1. Microstructure

The XRD patterns of the annealed $TiZrTa_xNbMo$ (x = 1.0, 0.9, 0.8, 0.7, and 0.6 at%) RHEAs are shown in Fig. 2. The BCC1 and BCC2 phases were observed in all the specimens. The diffraction peaks does not indicate the formation of an ordered BCC phase or an intermetallic compound phase. Table 1 shows the experimental density ($\rho_{exp}$) of $TiZrTa_xNbMo$ RHEAs, and the theoretical density ($\rho_{mix}$), as calculated using the following equation:

$$\rho_{\mathrm{mix}} = \frac{\sum_{i=1}^{n} c_i A_i}{\sum_{i=1}^{n} \frac{c_i A_i}{\rho_i}} \quad (1)$$

where $c_i$ is the atomic fraction of an element, $i$, $A_i$ is the relative atomic weight , $\rho_i$ is the density of an element, $i$. The results show that the experimental density was higher than the theoretical density.

The SEM morphologies of the annealed $TiZrTa_xNbMo$ RHEAs are displayed in Fig. 3. These micrographs show that all the alloys exhibit a dendritic structure, which is caused by high component undercooling during the solidification process. The formation of the dendritic structure also indicates the redistribution of elements. As shown in Fig. 3(a), the BCC1 phase in the dendritic arm region and the BCC2 phase in the

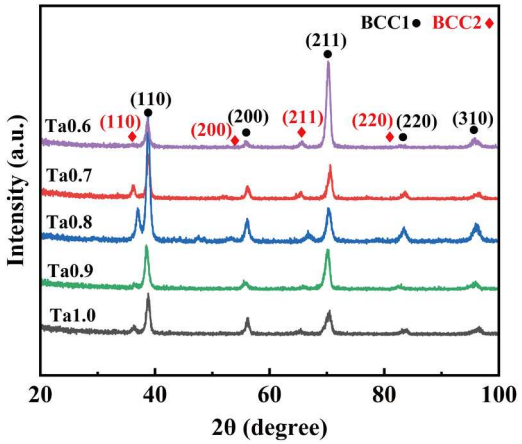


**Fig. 2.** XRD patterns of annealed $TiZrTa_xNbMo$ RHEAs.

**Table 1**
Density of the $TiZrTa_xNbMo$ RHEAs.

| Alloy | $\rho_{exp}$ (g/cm$^3$) | $\rho_{mix}$ (g/cm$^3$) |
|---|---|---|
| Ta1.0 | 9.29 ± 0.07 | 9.17 |
| Ta0.9 | 9.16 ± 0.05 | 9.05 |
| Ta0.8 | 9.02 ± 0.04 | 8.91 |
| Ta0.7 | 8.87 ± 0.02 | 8.74 |
| Ta0.6 | 8.68 ± 0.06 | 8.57 |

interdendritic region can be seen. Nevertheless, the dense dendritic structure induces the uneven distribution of the BCC2 phase in a small number of regions. With the decrease in the Ta content, more interdendritic regions begain to form. In contrast to the continuous elongated strip dendritic structure in the Ta0.7 alloy (Fig. 3(d)), irregular blocky dendritic arms divided by interdendrites can be seen in the Ta0.6 alloy (Fig. 3(e)), which further indicated that a decrease of Ta content significantly alters the morphology and content of the dendrites. The volume fraction of the BCC1 phase in $TiZrTa_xNbMo$ RHEAs was estimated using Image J software, as presented in Fig. 3(f). It is found that the volume fraction of the BCC1 phase gradually decreased from 89.5 % for Ta1.0 to 77.2 % for Ta0.6, indicating that it appeared that Ta decreases the stability of the BCC1 phase in the alloy.

The EDS-mapping results for the $TiZrTa_xNbMo$ RHEAs are presented in Fig. 4. In this figure, the results indicated that the elemental segregation occurred, which is caused by non-equilibrium solidification. Table 2 shows the elemental compositions of dendritic arms ($C_{da}$) and the interdendritic region ($C_{idr}$), with the average concentration of the element ($C_{aver}$) and the segregation coefficient (K). The dendritic arms regions contain high concentrations of Ta, Nb, and Mo, whereas the interdendritic regions are enriched with Ti and Zr. It is well known that when the K is farther from 1, compositional segregation can be severe. Comparing the K values of the various RHEAs, the segregation degree of Ta is greater than that of the other four elements.

Due to the limited resolution of the SEM, the microstructure of the Ta0.7 and Ta1.0 alloys were characterized in detail by TEM, as shown in Fig. 5. The bright-field (BF) images of Ta1.0 and Ta0.7 alloys are shown in Fig. 5(a) and (e), respectively. The selected-area electron diffraction (SAED) patterns of A, B, C, and D, which corresponds to Fig. 5(b), (c), (f), and (g), respectively, indicated that the alloys contain two BCC solid solution phases, which is consistent with the XRD results. The dark-field (DF) images in Fig. 5(d) and (h) clearly show that the BCC2 phase is well distributed within the BCC1 phase.

Fig. 6(a) and (d) exhibit the high-resolution transmission electron microscope (HRTEM) images at the interface of Ta1.0 and Ta0.7 alloys, respectively. The difference in contrast reflects the different distribution of elements in the alloy [31,32]. The lattice parameters of the BCC1 and BCC2 phases in the Ta1.0 alloy are 3.274 Å and 3.357 Å, respectively, while the lattice parameters of the BCC1 and BCC2 phases in the Ta0.7 alloy are 3.306 Å and 3.351 Å, respectively. The lattice parameter of the BCC1 phase in the Ta1.0 alloy is smaller than that of the Ta0.7 alloy, which indicates that the variation in the Ta content had a greater effect on the BCC1 phase. The lattice mismatch of the alloy can be calculated, $\varepsilon = 2(a_{BCC2} - a_{BCC1})/(a_{BCC1} + a_{BCC2})$, where $a_{BCC1}$ and $a_{BCC2}$ are the lattice parameters of the BCC1 and BCC2 phases, respectively.

The lattice mismatches of Ta1.0 and Ta0.7 alloys are 1.21 % and 0.67 %, respectively. Fig. 5(b) and (e) show the Inverse Fast Fourier Transform (IFFT) images of Ta1.0 and Ta0.7 alloys, respectively. It can be seen that the lattice mismatch of the Ta1.0 alloy is significantly greater than that of the Ta0.7 alloy, which is consistent with the calculated results. The lattice deformation of the alloy is more vividly described by the Geometric Phase Analysis (GPA) [33], as shown in Fig. 5(e) and (f). Compared to the Ta0.7 alloy, the lattice-strain distribution of the Ta1.0 alloy is more uneven, revealing a more severe lattice distortion that is caused by the high Ta content.

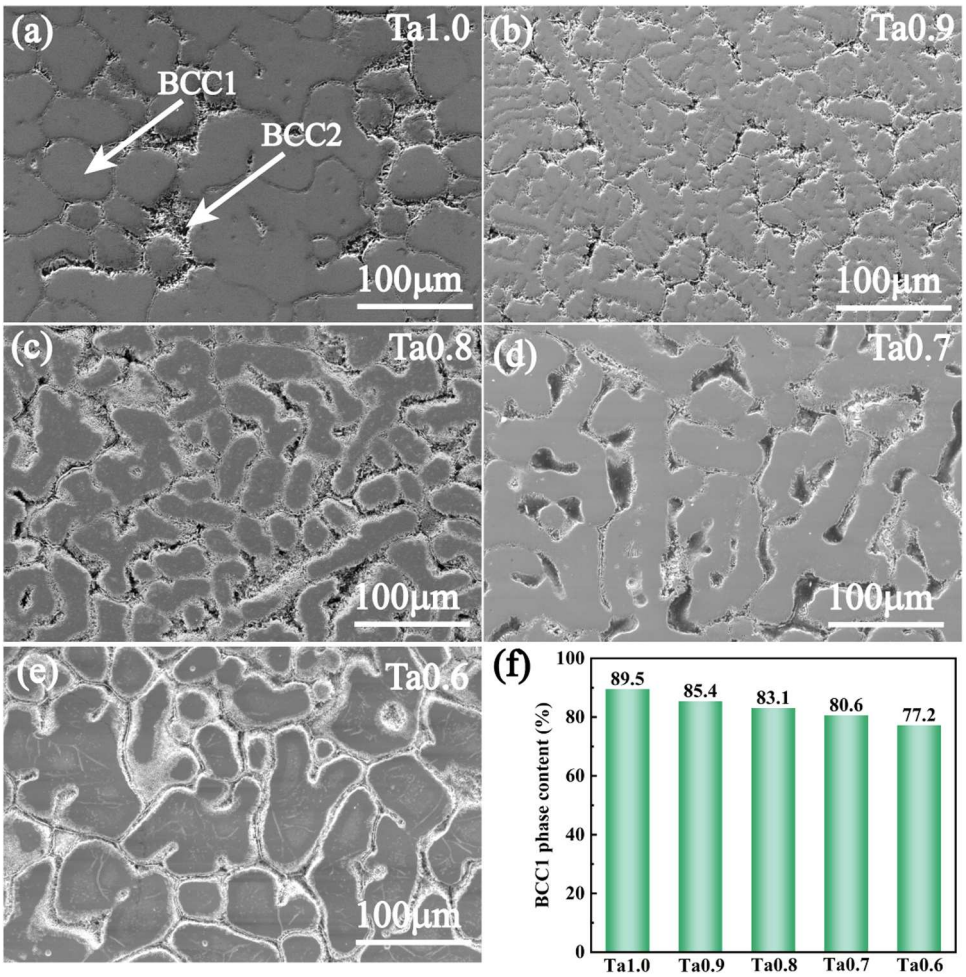


**Fig. 3.** SEM-BSE images of $TiZrTa_xNbMo$ RHEAs and volume fraction of the BCC1 phase, (a) Ta1.0, (b) Ta0.9, (c) Ta0.8, (d) Ta0.7, (e) Ta0.6, and (f) volume fraction of the BCC1 phase.

### 3.2. Mechanical properties

The compressive stress-strain curves of the $TiZrTa_xNbMo$ RHEAs at room temperature are displayed in Fig. 7(a). In addition, the resulting compression mechanical properties are summarized in Table 3. The errors values were calculated to ensure the accuracy of the data. In general, the errors values can be represented by standard deviations. The standard deviation is defined as the square root of the arithmetic mean of the square of the deviation between the standard value of each unit and its average. It reflects the degree of dispersion between individuals within the group. The standard deviation ($S$) can be obtained by the following equation:

$$S = \sqrt{\frac{\sum (X_i - \overline{X})^2}{n-1}} \quad (2)$$

where $X_i$ is the value of sample $i$, $\overline{X}$ is the mean value of the samples, and n is the number of samples. By inputting the test data into the origin software, the standard error value can be obtained quickly. The errors values in the Table 3 were expressed in bold font to distinguish more clearly.

As the Ta content decreases, the yield strength of the $TiZrTa_xNbMo$ RHEAs reduces from 1536 MPa for the Ta1.0 alloy to 1168 MPa for the Ta0.7 alloy. However, the plastic strain of the $TiZrTa_xNbMo$ RHEAs greatly increases from 9.1 % for the Ta1.0 alloy to 34.8 % for the Ta0.7 alloy. Although the plasticity of the Ta0.6 alloy decreases, it is still significantly higher than that of the Ta1.0 alloy. The variation of microhardness is similar to that of the yield strength, as shown in Fig. 7 (b). Fig. 7(c) shows the comparison of yield strength and strain between $TiZrTa_xNbMo$ RHEAs in this work and other similar alloys. Obviously, the $Ti_{30}Zr_{30}Nb_{20}Ta_{20}$ alloy was located at the top left of the figure, which indicates that it has high yield strength, but the plasticity is low. Similarly, TiZrNbTa alloy have a plasticity of ~50 % but insufficient yield strength. By contrast, the Ta0.7 alloy exhibit excellent plastic-deformation behavior and maintained a high yield strength.

In general, the microstructure of an alloy is closely related to its mechanical properties. The decrease of the Ta content leads to the increase of the BCC2 phase formed in the interdendritic region. During the stress-loading process, the initiation of deformation bands is promoted in the brittle-dendrite region. When the deformation bands expanded further, they are hindered by the interdendritic region, which enhances the plasticity of the alloy [34]. It is worth noting that an excess of the BCC2 phase divides the BCC1 phase (Fig. 3(e)), resulting in low deformation synergy, which is a crucial reason for the decrease in the plasticity of the Ta0.6 alloy. However, its decrease in yield strength and hardness can be attributed to the degradation of the solid-solution strengthening that is caused by reducing the Ta content, which will be discussed in detail in Section 4.3.

### 3.3. Deformation evolution

Fig. 8 presents the TEM images of the Ta0.7 alloy at various strain conditions. Before the deformation process began (0 %), there is no obvious dislocation in the alloy, as shown in Fig. 8(a). During plastic

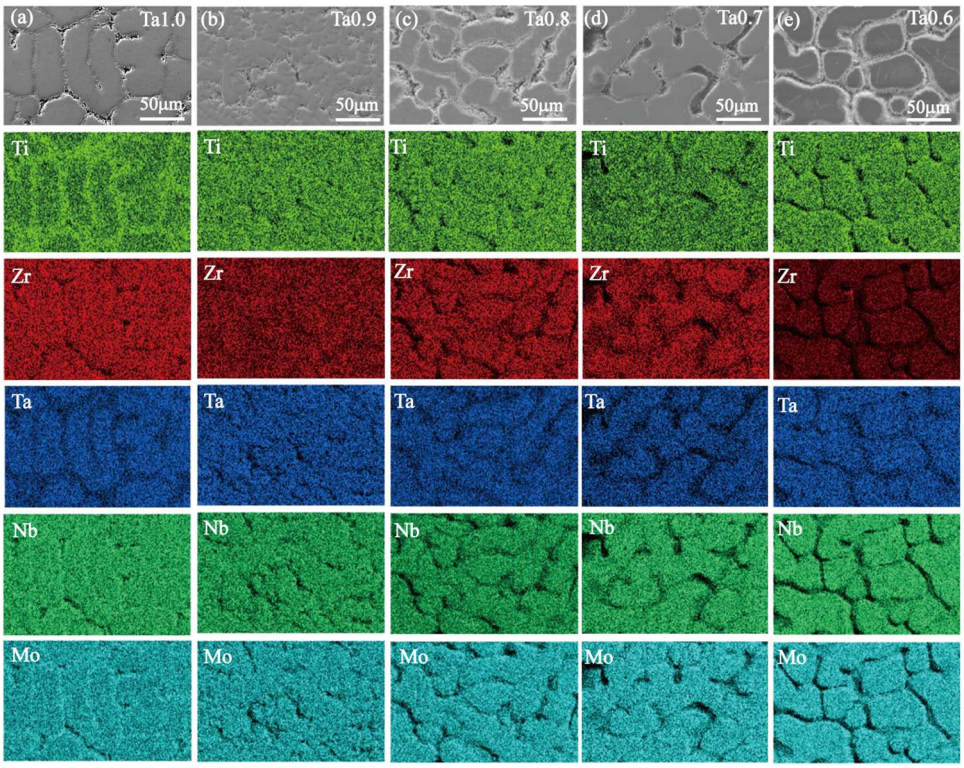


**Fig. 4.** EDS mapping of $TiZrTa_xNbMo$ RHEAs: (a) Ta1.0 , (b) Ta0.9 , (c) Ta0.8 , (d) Ta0.7 , (e) Ta0.6.

**Table 2**
Chemical compositions of the $TiZrTa_xNbMo$ RHEAs (at%).

| Alloys | | Ti | Zr | Ta | Nb | Mo |
|---|---|---|---|---|---|---|
| Ta1.0 | $C_{da}$ | 3.68 | 5.84 | 41.31 | 20.21 | 28.96 |
| | $C_{idr}$ | 23.78 | 41.52 | 10.82 | 11.57 | 12.31 |
| | $C_{aver}$ | 22.02 | 20.84 | 19.36 | 18.48 | 19.30 |
| | $K = C_{da}/C_{idr}$ | 0.15 | 0.14 | 3.82 | 1.75 | 2.35 |
| Ta0.9 | $C_{da}$ | 4.86 | 7.79 | 38.37 | 21.85 | 27.13 |
| | $C_{idr}$ | 23.40 | 42.37 | 9.56 | 12.09 | 12.58 |
| | $C_{aver}$ | 21.35 | 22.68 | 17.41 | 18.52 | 20.04 |
| | $K = C_{da}/C_{idr}$ | 0.21 | 0.18 | 4.01 | 1.81 | 2.16 |
| Ta0.8 | $C_{da}$ | 6.51 | 11.52 | 31.61 | 22.54 | 27.82 |
| | $C_{idr}$ | 24.81 | 44.56 | 8.79 | 12.42 | 9.42 |
| | $C_{aver}$ | 22.35 | 23.71 | 16.24 | 18.13 | 19.57 |
| | $K = C_{da}/C_{idr}$ | 0.26 | 0.26 | 3.40 | 1.81 | 2.95 |
| Ta0.7 | $C_{da}$ | 6.25 | 12.04 | 29.08 | 24.42 | 28.21 |
| | $C_{idr}$ | 26.41 | 45.72 | 6.74 | 11.57 | 9.56 |
| | $C_{aver}$ | 20.60 | 21.05 | 14.52 | 23.01 | 20.82 |
| | $K = C_{da}/C_{idr}$ | 0.24 | 0.26 | 4.31 | 2.11 | 2.95 |
| Ta0.6 | $C_{da}$ | 6.71 | 13.55 | 26.37 | 24.25 | 29.12 |
| | $C_{idr}$ | 27.06 | 46.02 | 6.04 | 11.10 | 8.78 |
| | $C_{aver}$ | 19.62 | 23.58 | 14.17 | 20.25 | 22.38 |
| | $K = C_{da}/C_{idr}$ | 0.25 | 0.29 | 4.35 | 2.18 | 3.31 |

deformation, a small number of dislocations were observed in the alloy at the plastic strain of 12 %, as depicted in Fig. 8(b). When the strain further increased to 24 %, the number of dislocations increased, and dislocation tangles appeared (Fig. 8(c)). When the stress was loaded until fracture (34.8 %), as shown in Fig. 8(d), planar-slip bands were also observed in the alloy, which was similar to the results reported by Zhang et al. [37]. Due to the high friction stress, the undissociated dislocations in the alloy must overcome the continuous energy barrier to move, which leads to its orderly accumulation and the formation of a slip band structure. The regular dislocations in these slip bands moved very slowly. As the fast-moving partial dislocation moves towards the slip-band direction (indicated by the red arrow in Fig. 8(d)), the slip bands hinder partial dislocations. The motion of these dislocations requires additional force to overcome. The mutual entanglement between dislocations and their interaction with slip bands lead to a high work-hardening capability of the alloy. During the room-temperature compression process, the deformation mode of the alloy is always toward a dislocation slip, without the activation of other additional deformation mechanisms, such as stress-induced martensitic transformation and twinning. This feature is related to the high stacking fault energy and great matrix phase stability of the alloy [38].

## 4. Discussion

### 4.1. Phase-formation criteria

Since the design concept of high-entropy alloy is very different from that of traditional alloy, the study of the formation of a solid solution is the essential work in the development of such alloys [39]. However, the conventional Hume-Rothery rules can predict the phase composition in the binary alloy system, but it is not suitable for multi-principal HEAs. Thus, Zhang et al. [40] proposed a novel rule for predicting phase formation in HEAs and introduced three physical parameters: the mixing entropy ($\Delta S_{mix}$), mixing enthalpy ($\Delta H_{mix}$), and atomic-radius difference ($\delta$). These parameters are expressed as follows:

$$\Delta S_{mix} = -R\sum_{i=1}^{N}(c_i \ln c_i) \tag{3}$$

$$\Delta H_{mix} = \sum_{i=1,i\neq j}^{n} \Omega_{ij} c_i c_j = \sum_{i=1,i\neq j}^{n} 4\Delta H_{ij}^{mix} c_i c_j \tag{4}$$

$$\delta = \sqrt{\sum_{i=1}^{n} c_i \left(1 - r_i \Big/ \left(\sum_{i=1}^{n} c_i r_i\right)\right)^2} \times 100\% \tag{5}$$

where R (8.314 J/K/mol) is the molar gas constant, $c_i$ is the atomic fraction of an element, $i$, $r_i$ is the atomic radius of an element $i$, $\Delta H_{ij}$ represents the mixing enthalpy between elements $i$ and $j$, as shown in

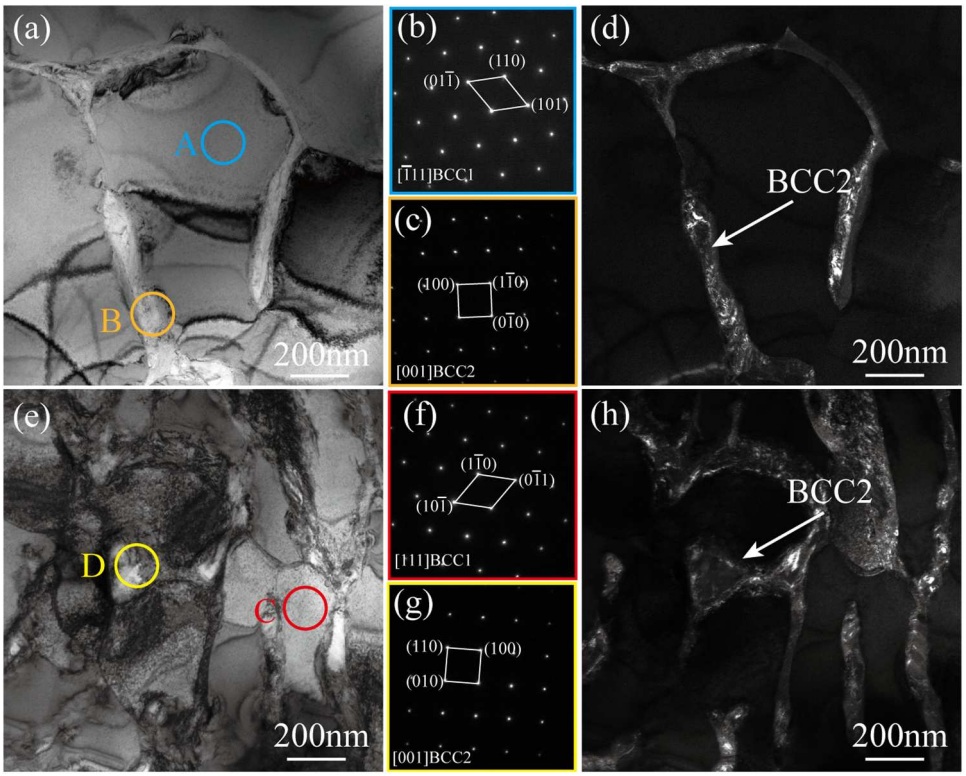


**Fig. 5.** TEM characterization of Ta1.0 and Ta0.7 alloys, (a) BF TEM image of Ta1.0 alloy. (b, c) SAED patterns of A and B, (d) DF TEM image of BCC2 phase for Ta1.0 alloy, (e) BF TEM image of Ta0.7 alloy, (f, g) SAED patterns of C and D, (h) DF TEM image of BCC2 phase for Ta0.7 alloy.

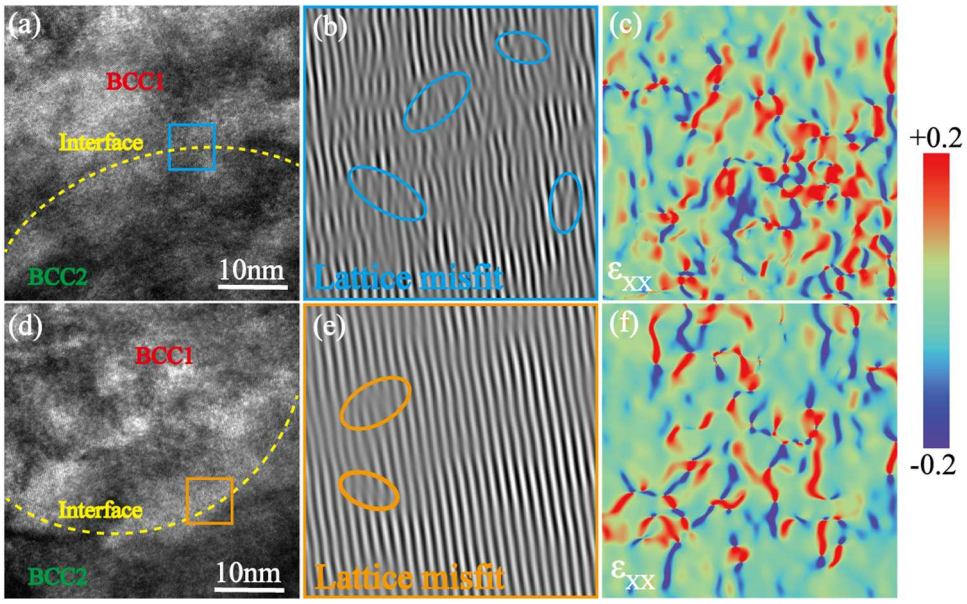


**Fig. 6.** HRTEM images of (a) Ta1.0 and (d) Ta0.7 alloys, (b) and (e) are the enlarged images of the red and yellow square regions in (a) and (d), respectively, (c) and (f) are the IFFT images of (b) and (e), respectively.

Fig. 9. Although the high mixing entropy in HEAs hinders the formation of intermetallic compounds, it cannot offset the contribution of mixing enthalpy to free energy. From the thermodynamic point of view, the mixing enthalpy can promote the formation of intermetallic compounds. However, due to the small binary mixing enthalpy in the TiZrTa$_x$NbMo RHEAs system, it is difficult to form intermetallic compounds.

Moreover, to enrich the new solid-solution formation criterion and accurately describe the relationship between $S_{mix}$ and $\Delta H_{mix}$, Yang et al. [42] presented a new parameter ($\Omega$), which is defined as follows:

$$\Omega = \frac{T_m^{mix}\Delta S_{mix}}{|\Delta H_{mix}|} \tag{6}$$

where $T_m^{mix}$ is the theoretical melting temperature of the alloy, which can be calculated using the rule of mixtures (ROM):

$$T_m^{mix} = \sum c_i (T_m)_i \tag{7}$$

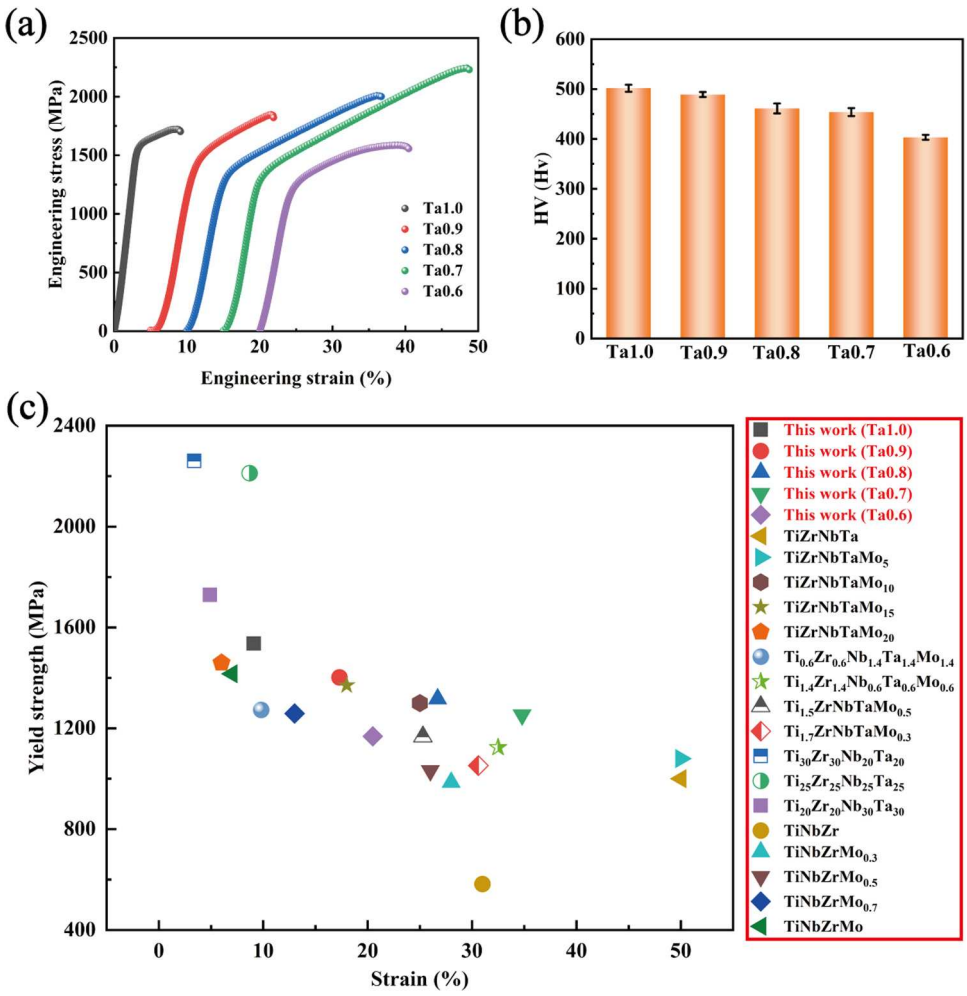


**Fig. 7.** (a) Engineering stress-strain curves and (b) Vickers hardness of TiZrTa$_x$NbMo RHEAs. (c) Mechanical properties of this work compared with previous reports Refs [21,22,35,36].

**Table 3**
Mechanical properties of TiZrTa$_x$NbMo RHEAs.

| Alloys | Yield strength (MPa) | Plastic strain (%) | Vickers hardness (Hv) |
|---|---|---|---|
| Ta1.0 | 1536 ± **38** | 9.1 ± **1.2** | 501.7 ± **7.2** |
| Ta0.9 | 1402 ± **25** | 17.3 ± **2.7** | 489.1 ± **4.8** |
| Ta0.8 | 1317 ± **17** | 26.7 ± **1.5** | 461.2 ± **10.6** |
| Ta0.7 | 1253 ± **23** | 34.8 ± **4.1** | 453.9 ± **8.2** |
| Ta0.6 | 1168 ± **16** | 20.5 ± **2.6** | 403.2 ± **4.7** |

where $(T_m)_i$ is the melting point of element *i*.

According to the previous experimental results [42], the disordered solid-solution-formation rule is determined to be $-15 \leq \Delta H_{mix} \leq 5$ kJ/mol and $\delta \leq 5$ %. When $\Omega \geq 1.1$ and $\delta \leq 6.6$ %, it is beneficial to the formation of a single-phase solid solution.

In addition, Guo et al. [43,44] presented a concept to evaluate the stability of phase by the valence electron concentration (*VEC*), which can be expressed as:

$$VEC = \sum_{i=1}^{N} c_i (VEC)_i \tag{8}$$

where $(VEC)_i$ is the *VEC* of an element, *i*. According to the findings of Guo [43], when the *VEC* < 6.87, the BCC solid solutions are formed, while the FCC solid solutions tend to be generated when the *VEC* ≥ 8. Table 4 shows the related parameters of the elements in TiZrTa$_x$NbMo RHEAs.

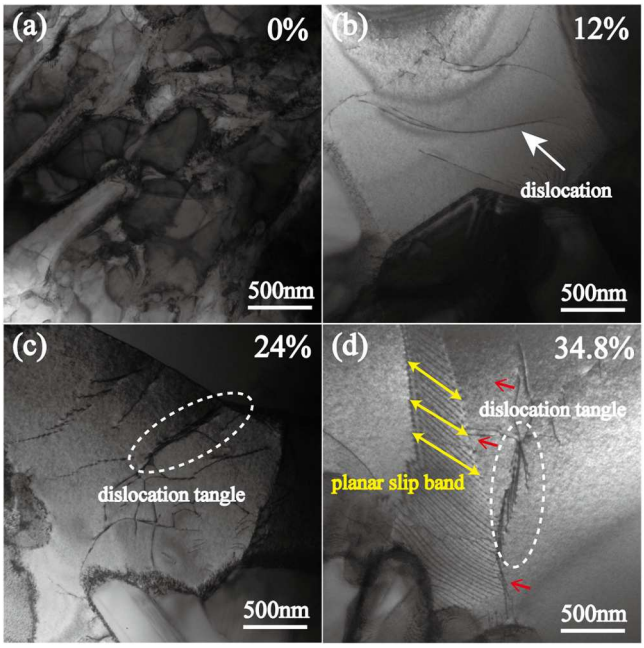


**Fig. 8.** TEM images of the Ta0.7 alloy under different strains: (a) 0 %, (b) 12 %, (c) 24 %, (d) 34.8 %.

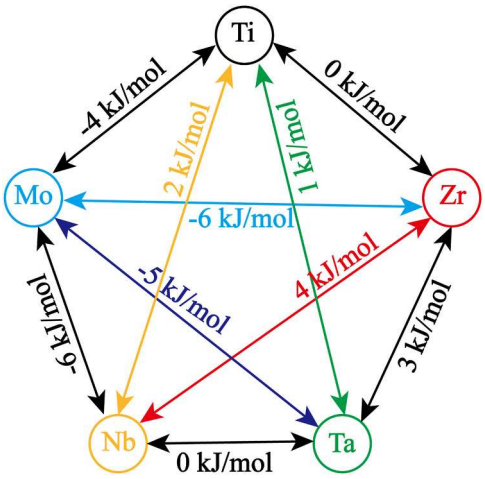


**Fig. 9.** $\Delta H_{mix}$ of every two elements in TiZrTa$_x$NbMo RHEAs [41].

**Table 4**
Related parameters of the elements in TiZrTa$_x$NbMo RHEAs [45].

| Element | Ti | Zr | Ta | Nb | Mo |
|---|---|---|---|---|---|
| Atomic radius , $r$ (nm) | 0.147 | 0.160 | 0.147 | 0.147 | 0.140 |
| Lattice parameter, $a$ (nm) | 0.3276 | 0.3582 | 0.3303 | 0.3301 | 0.3147 |
| Young's modulus, $E$ (GPa) | 116 | 88 | 186 | 105 | 329 |
| Shear modulus, $G$ (GPa) | 44 | 33 | 69 | 38 | 126 |
| Valence electron concentration, *VEC* | 4 | 4 | 5 | 5 | 6 |
| Vickers hardness, HV(Hv) | 99 | 92 | 89 | 135 | 156 |
| Yield strength, $\sigma_{0.2}$ (MPa) | 195 | 280 | 170 | 240 | 420 |
| Melting temperature, $T_m$ (K) | 1941 | 2128 | 3290 | 2750 | 2893 |

The physical parameters calculated using the empirical formula are shown in Table 5. It is noted that the TiZrTa$_x$NbMo RHEAs form a BCC structure when the VEC values are far less than 6.87, which is consistent with the results of XRD and TEM for this alloy. Furthermore, the $\Delta H_{mix}$ values are between −15 ~ 5 kJ/mol, and δ values are less than 5 %, which causes the formation of a disordered solid solution. Although the Ω values are greater than 1.1, and δ values are less than 6.6 %, it does not form a single-phase solid solution but a dual-phase solid solution, which is inconsistent with the empirical formula. This trend shows that the solid-solution formation rule cannot completely predict the phase composition of TiZrTa$_x$NbMo RHEAs.

It is not conclusive to judge the phase composition of TiZrTa$_x$NbMo RHEAs only by phase-formation rules. Therefore, the equilibrium solidification phase diagrams of the Ta1.0 and Ta0.7 alloys were calculated, using the Thermo-Calc software (TCNI-5 database), as presented in Fig. 10(a) and (b). The BCC phase region initially formed at 2300 °C. When the temperature reduced to about 1250 °C, a second BCC2 phase began to form, which was caused by the final solidification of elements with lower melting point. It is worth noting that the HCP phase appears in the phase diagram at 500 °C. However, no formation of this phase was observed by experimental characterization. There are two main reasons for the difference between the phase-diagram calculation results and the experimental results. On one hand, the database does not accurately reflect the relationship between the elements. On the other hand, the rapid cooling rate after arc melting results in insufficient time for the BCC phase to transform into the HCP phase.

**Table 5**
Calculated parameters of TiZrTa$_x$NbMo RHEAs.

| Alloys | $\Delta H_{mix}$ (kJ/mol) | $\Delta S_{mix}$ (J/mol/K) | $T_m^{mix}$ (K) | $\Omega$ | $\delta$ (%) | *VEC* |
|---|---|---|---|---|---|---|
| Ta1.0 | -1.76 | 13.38 | 2600 | 19.77 | 4.38 | 4.8 |
| Ta0.9 | -2.05 | 13.37 | 2587 | 16.87 | 4.43 | 4.796 |
| Ta0.8 | -2.17 | 13.35 | 2573 | 15.82 | 4.47 | 4.792 |
| Ta0.7 | -2.36 | 13.31 | 2556 | 14.41 | 4.53 | 4.787 |
| Ta0.6 | -2.49 | 13.24 | 2540 | 13.50 | 4.57 | 4.7825 |

### 4.2. Elemental microsegregation

Generally, elemental microsegregation in HEA is related to the uneven distribution of its chemical composition during solid-solution solidification. To investigate the elemental microsegregation, Senkov et al. [10] presented the parameter, $\Delta C = C_{da} - C_{aver}$, and the parameter, $\Delta T = (T_m)_i - T_m{}^{\text{mix}}$, and established a linear relationship between them. Nevertheless , this linear relationship is only suitable for equimolar alloys because the variation of molar ratios causes a deviation of the equation. Therefore, the new parameter, $\delta C = (C_{da} - C_{aver})/C_{aver}$, proposed by Ge was adopted [46], which has the following relationship with $\Delta T$:

$$\delta C = k\Delta T \tag{9}$$

where $k$ is a constant. It is noted that the greater the absolute value of δC, the more severe the elemental segregation in the alloy. In the equilibrium-solidification process, the infinitely slow cooling rate causes the atoms to sufficiently diffuse. Hence, the δC values should be 0. However, under actual conditions, for the elements with $T_m > T_m^{mix}$, their $\delta C > 0$, while for the elements with $T_m < T_m^{mix}$, $\delta C < 0$.

Fig. 11 shows the linear relationship between $\delta C$ and $\Delta T$ where the ellipses of different colors represent concentrated areas of each element. It can be seen that the first quadrant of the axial scattering diagram contains the high-melting temperature elements, Ta, Mo, and Nb, which indicates that they are preferentially segregated during solidification and enriched in the dendritic-arm region. Nevertheless, Ti and Zr are distributed in the third quadrant, which means that they are the final solidified elements and accumulated in the interdendritic region. The fitted slope, $k$, can be used as a criterion to evaluate the degree of elemental microsegregation in the alloy. The $k$ values of Ta1.0, Ta0.9, Ta0.8, Ta0.7, and Ta0.6 are 1.58 × $10^{-3}$, 1.43 ×$10^{-3}$, 1.23×$10^{-3}$, 1.18×$10^{-3}$ and 1.09×$10^{-3}$, respectively, indicating that the decrease of the Ta content weakens the degree of segregation. Since Ta has the highest melting point (~ 3290 K) compared to other elements of TiZrTa$_x$NbMo RHEAs, the liquidus-solidus interval expands with the increase of the Ta content, which provides sufficient solidification time for the growth of dendritic arms. In addition, due to the slow diffusion mechanism, the higher Ta content reduces the diffusion rate of atoms, which eventually aggravates the segregation process. Therefore, appropriately decreasing the Ta content in the HEA is beneficial to reduce elemental segregation.

### 4.3. Solid-solution strengthening

In the initial stage of alloy development, the yield strength and microhardness can be roughly evaluated by the ROM, which are expressed as $\sigma_{0.2}^{mix\text{-}cal}$ and $HV^{mix\text{-}cal}$, respectively, shown as follows:

$$\sigma_{0.2}{}^{mix-cal} = \sum c_i(\sigma_{0.2})_i \tag{10}$$

$$HV^{mix-cal} = \sum c_i(HV)_i \tag{11}$$

where $(\sigma_{0.2})_i$ and $(HV)_i$ are the yield strength and microhardness of an element, $i$, in the alloy, respectively.

Obviously, the ROM is not suitable for calculating the strength and hardness of TiZrTa$_x$NbMo RHEAs, as exhibited in Fig. 12. The calculated $\sigma_{0.2}^{mix\text{-}cal}$ and $HV^{mix\text{-}cal}$ are significantly lower than the respective experimental $\sigma_{0.2}^{exp}$ and $HV^{exp}$. Similar findings have been reported in previously reported research [47,48]. These results suggest that the superior strength and hardness of the alloy are caused by the

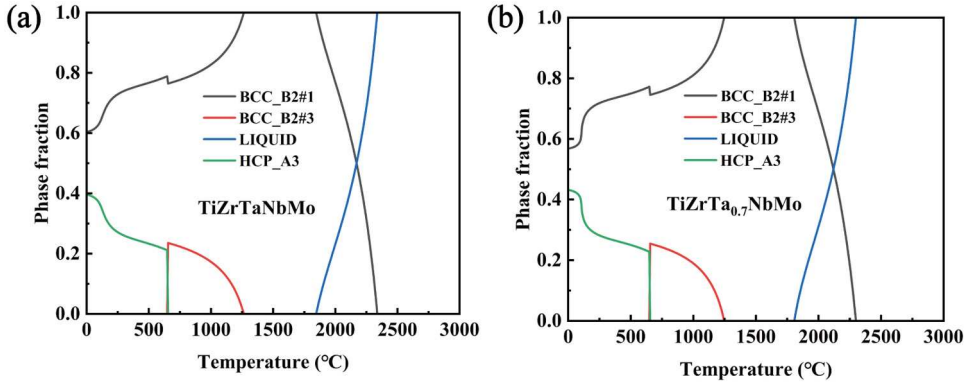


**Fig. 10.** Equilibrium solidification phase diagrams of (a) Ta1.0 and (b) Ta0.7 alloys.

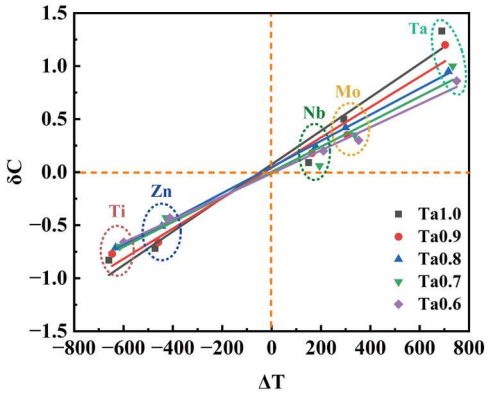


**Fig. 11.** Correlation between $\delta C$ and $\Delta T$ of TiZrTa$_x$NbMo RHEAs.

solution-strengthening mechanism [49].

The solute atoms dissolve into the matrix phase to form a solid-solution structure, which is a prerequisite for the solid-solution strengthening of the alloy. The lattice distortion caused by the difference in atomic radius will hinder the dislocation, which significantly enhances the strength and hardness of the alloy. In general, the solid-solution strengthening can be attributed to the interaction between solute atoms and dislocations [50]. The magnitude of the interaction force (F) can be expressed by the following equation:

$$F = Gb^2 f \tag{12}$$

where $G$ is the shear modulus of the alloy, $b$ is the magnitude of the Burgers vector, and $f$ is the mismatch parameter. The solid-solution strengthening effect can be defined as :

$$\Delta\sigma b^2 = ZF^{4/3}c^{2/3}E_L{}^{-1/3} \tag{13}$$

where $Z$ is a material-dependent dimensionless constant, $c$ is the solute concentration, and $E_L$ is the dislocation-line tension. Combining Eqs. (12) and (13), and using the expression, $E_L = Gb^2/2$, the solute-induced stress can be estimated as:

$$\Delta\sigma_{\mathrm{i}} = \mathrm{A}G\mathrm{f}_i^{4/3}\mathrm{c}_i^{2/3} \tag{14}$$

where A is a dimensionless material constant, and the parameter, $f_i$, can be expressed as:

$$\mathrm{f}_{\mathrm{i}} = \sqrt{{\delta_{Gi}}^2 + \alpha^2{\delta_{\mathrm{ri}}}^2} \tag{15}$$

where $\delta_{Gi}$ is $\delta_{ri}$ are the modulus mismatch and atomic-size mismatch of the element, $i$, in the alloy, respectively. $\alpha$ is a physical constant, which can be determined by the category of mobile dislocations. In general, α values larger than 16 are for edge dislocations, whereas an α value is between 2 and 4 represents screw dislocations. Since to the dislocation type for the RHEAs was mainly edge dislocation [51–54], the $\alpha$ value was set to be 16.

In the ideal state, it is assumed that the RHEA is a uniform solid-solution structure, and each solute in the lattice and its eight nearest neighboring atoms form nine atomic clusters. The modulus mismatch and atomic-size mismatch between the solute and solvent lead to the lattice distortion around solute atoms. $\delta_{Gi}$ and $\delta_{ri}$ of an element, $i$, respectively, are defined by:

$$\delta_{Gi} = {}^{9/8}\sum c_j\delta_{Gij} \tag{16}$$

$$\delta_{ri} = {}^{9/8}\sum \mathrm{c}_j\delta_{\mathrm{rij}} \tag{17}$$

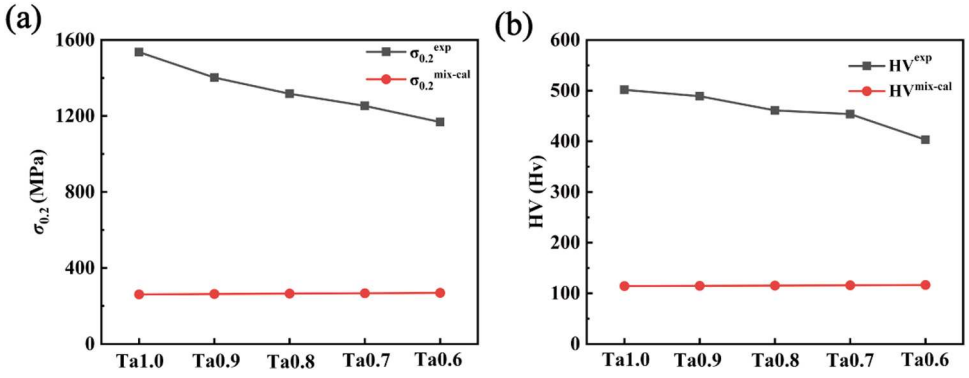


**Fig. 12.** Relationship between calculated values and experimental values of TiZrTa$_x$NbMo RHEAs: (a) $\sigma_{0.2}^{mix\text{-}cal}$- $\sigma_{0.2}^{exp}$, (b) $HV^{mix\text{-}cal}$- $HV^{exp}$.

where $c_j$ is the atomic fraction of an element, $j$, $\delta_{Gij} = 2(G_i - G_j)/(G_i + G_j)$ is the atomic-modulus difference between elements, $i$ and $j$, and $\delta_{rij} = 2(r_i - r_j)/(r_i + r_j)$ is the atomic-size difference between elements, $i$ and $j$.

The calculated $\delta_{Gij}$ and $\delta_{rij}$ values are summarized in Table 6. The spectrum of $\delta_{Gij}$ values for the alloying elements is extremely wide, ranging from 0.082 for the Nb-Zr atom pair to 1.130 for the Mo-Zr atom pair. The atomic pairs of Mo and other elements causes the highest shear modulus impact ($\delta_{Gij}$ = 0.585 for Mo-Ta to $\delta_{Gij}$ = 1.130 for Mo-Zr). Similarly, the data in Table 6 shows that the largest difference in the atomic size is between the Mo and Zr pair ($\delta_{rij}$ = 0.133).

The solid-solution strengthening effect ($\Delta\sigma$) of the alloy is not linearly superimposed, but can be estimated according to the following formula:

$$\Delta\sigma = \left(\sum \Delta\sigma_i^{3/2}\right)^{2/3} \tag{18}$$

Thus, the theoretical yield strength of the alloy can be obtained below:

$$\boldsymbol{\sigma}_{0.2}^{cal} = {\sigma_{0.2}}^{mix-cal} + \boldsymbol{\Delta\sigma} \tag{19}$$

The yield strength of the TiZrTa$_x$NbMo RHEAs can be calculated using this theoretical model, and the calculated values and experimental values were plotted as shown in Fig. 13. It is found that the calculated values of yield strength are higher than the experimental values, but the maximum deviation is less than 15 %. The difference in yield-strength values can be attributed to the fact that the thermal-activation process is not considered in the calculation, which can alleviate deformation and decrease stress. Therefore, the model is relatively accurate for analyzing the room-temperature yield strength and hardness [55,56]. In addition, it should be noted that the yield strength is mainly derived from solid-solution strengthening.

As a new type of metal material, the development of TiZrTa$_x$NbMo RHEAs is a long process from experimental verification to practical application. First of all, it is necessary to optimize the alloy composition and select the appropriate preparation method to ensure that it has excellent mechanical properties. Secondly, through thermal mechanical processing, good processing performance is obtained, and the performance index of engineering application materials is further achieved. Finally, considering the cost and economic benefits, it is evaluated whether the optimized alloy can be put into actual production. According to the current situation, TiZrTa$_x$NbMo RHEAs are not mature enough and have been in the research and development process. However, we believe that TiZrTa$_x$NbMo RHEAs will be applied in the real world in the near future.

## 5. Conclusions

In summary, the microstructure and mechanical properties of a series of TiZrTa$_x$NbMo RHEAs were investigated, and the corresponding strengthening mechanism was discussed. The following conclusions can be drawn from the results of the present work:

(1) TiZrTa$_x$NbMo RHEAs with a typical dendritic structure are composed of main BCC1 and minor BCC2 phases. With the decrease of the Ta content in the alloy, the volume fraction of the BCC1 phase gradually decreases, and the dendritic arm structure changes from a dense to dispersed condition.
(2) Elemental microsegregation was observed in the alloy, which is caused by non-equilibrium solidification. The elements with higher melting points (Ta, Nb, and Mo) are enriched in the dendritic arm region, while the elements with lower melting points (Ti and Zr) are concentrated in the interdendritic region. With the decrease of the Ta content, the degree of elemental segregation gradually decreases.

**Table 6**
Atomic-modulus difference ($\delta_{Gij}$) and atomic-size difference ($\delta_{rij}$) of element pairs in the alloy.

| $i/j/\ \delta_{Gij}/\delta_{rij}$ | Ti | Zr | Ta | Nb | Mo |
|---|---|---|---|---|---|
| Ti | 0 | **-0.228** | **0.442** | **-0.146** | **0.965** |
| Zr | -0.085 | 0 | **0.654** | **0.082** | **1.130** |
| Ta | 0.085 | 0.085 | 0 | **-0.579** | **0.585** |
| Nb | 0 | 0.085 | 0 | 0 | **1.073** |
| Mo | 0.049 | 0.133 | 0.049 | 0.049 | 0 |

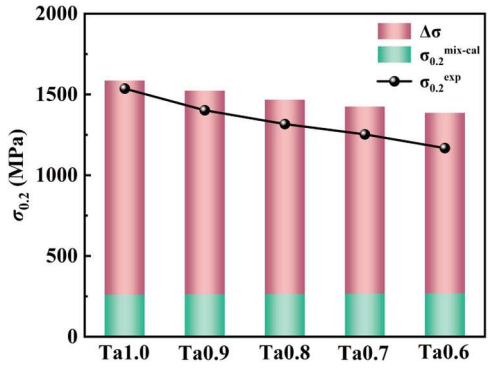


**Fig. 13.** Relationship between calculated and experimental values of yield strengths in TiZrTa$_x$NbMo RHEAs.

(3) At room temperature, as the decrease of Ta content, the plasticity of TiZrTa$_x$NbMo RHEAs increases significantly. The Ta0.7 alloy exhibit the highest plasticity, which is 34.8 %, while its yield strength is maintained at 1253 MPa.
(4) The variation in the yield strength and hardness of the TiZrTa$_x$NbMo RHEAs is mainly induced by the atomic-size mismatch and modulus mismatch, which can be explained by the solid-solution strengthening model. The calculated theoretical vaules for this alloy agree well with the experimentally obtained values.

## CRediT authorship contribution statement

**Binbin Wang:** Software. **Liangshun Luo:** Validation. **Yue Zhang:** Resources, Funding acquisition. **Chao Liu:** Validation. **Feng Liu:** Methodology. **Fuyu Dong:** Writing – review & editing, Project administration, Funding acquisition, Data curation. **Peter K. Liaw:** Visualization, Software. **Xiangyang Shen:** Writing – original draft, Methodology, Formal analysis, Conceptualization. **Zihe Guo:** Investigation, Formal analysis. **Jun Cheng:** Funding acquisition. **Xiaoguang Yuan:** Supervision. **Yanqing Su:** Validation.

## Declaration of Competing Interest

We declare that we have no financial and personal relationships with other people or organizations that can inappropriately influence our work, there is no professional or other personal interest of any nature or kind in any product, service and/or company that could be construed as influencing the position presented in, or the review of, the manuscript entitled “Microstructural evolution and mechanical behavior of novel TiZrTa$_x$NbMo refractory high-entropy alloys”.

## Data availability

The authors do not have permission to share data.

## Acknowledgements

The present work was supported by the National Natural Science

Foundation of China (52271249), Natural Science Foundation of Liaoning Province (2023JH2/101700276), the Grant Plan for Young and Middle-aged Innovation Scientists of Shenyang Government (RC210058), Basic Scientific Research Project of Education Department of Liaoning Province (LJKMZ20220466), Key Research and Development Program of Shaanxi (2023-YBGY-488), and Project supported by State Key Laboratory of Powder Metallurgy, Central South University, Changsha, China. P. K. Liaw very much appreciates the support from (1) the National Science Foundation (DMR-1611180, 1809640, and 2226508) and (2) the US Army Research Office (W911NF-13-1-0438 and W911NF-19-2-0049).

## References

[1] B. Cantor, I.T.H. Chang, P. Knight, A.J.B. Vincent, Microstructural development in equiatomic multicomponent alloys, Mater. Sci. Eng. A 375–377 (2004) 213–218.
[2] J.-W. Yeh, S.-K. Chen, S.-J. Lin, J.-Y. Gan, T.-S. Chin, T.-T. Shun, C.-H. Tsau, S.-Y. Chang, Nanostructured high-entropy alloys with multiple principal elements: novel alloy design concepts and outcomes, Adv. Eng. Mater. 6 (2004) 299–303.
[3] D.J.M. King, S.C. Middleburgh, A.G. McGregor, M.B. Cortie, Predicting the formation and stability of single phase high-entropy alloys, Acta Mater. 104 (2016) 172–179.
[4] D. Liu, P. Yu, G. Li, P.K. Liaw, R. Liu, High-temperature high-entropy alloys AlxCo15Cr15Ni70-x based on the Al-Ni binary system, Mater. Sci. Eng. A. 724 (2018) 283–288.
[5] C.-C. Juan, M.-H. Tsai, C.-W. Tsai, C.-M. Lin, W.-R. Wang, C.-C. Yang, S.-K. Chen, S.-J. Lin, J.-W. Yeh, Enhanced mechanical properties of HfMoTaTiZr and HfMoNbTaTiZr refractory high-entropy alloys, Intermetallics 62 (2015) 76–83.
[6] S. Alvi, F. Akhtar, High temperature tribology of CuMoTaWV high entropy alloy, Wear 426–427 (2019) 412–419.
[7] Y. Cao, Y. Liu, Y. Li, B. Liu, J. Wang, M. Du, R. Liu, Precipitation strengthening in a hot-worked TiNbTa0.5ZrAl0.5 refractory high entropy alloy, Mater. Lett. 246 (2019) 186–189.
[8] J.Y. He, H. Wang, H.L. Huang, X.D. Xu, M.W. Chen, Y. Wu, X.J. Liu, T.G. Nieh, K. An, Z.P. Lu, A precipitation-hardened high-entropy alloy with outstanding tensile properties, Acta Mater. 102 (2016) 187–196.
[9] H. Song, F. Tian, D. Wang, Thermodynamic properties of refractory high entropy alloys, J. Alloy. Compd. 682 (2016) 773–777.
[10] O.N. Senkov, G.B. Wilks, D.B. Miracle, C.P. Chuang, P.K. Liaw, Refractory high-entropy alloys, Intermetallics 18 (2010) 1758–1765.
[11] O.N. Senkov, G.B. Wilks, J.M. Scott, D.B. Miracle, Mechanical properties of Nb25Mo25Ta25W25 and V20Nb20Mo20Ta20W20 refractory high entropy alloys, Intermetallics 19 (2011) 698–706.
[12] J. Chen, X. Zhou, W. Wang, B. Liu, Y. Lv, W. Yang, D. Xu, Y. Liu, A review on fundamental of high entropy alloys with promising high–temperature properties, J. Alloy. Compd. 760 (2018) 15–30.
[13] C.-C. Juan, M.-H. Tsai, C.-W. Tsai, C.-M. Lin, W.-R. Wang, C.-C. Yang, S.-K. Chen, S.-J. Lin, J.-W. Yeh, Enhanced mechanical properties of HfMoTaTiZr and HfMoNbTaTiZr refractory high-entropy alloys, Intermetallics 62 (2015) 76–83.
[14] M. Todai, T. Nagase, T. Hori, A. Matsugaki, A. Sekita, T. Nakano, Novel TiNbTaZrMo high-entropy alloys for metallic biomaterials, Scr. Mater. 129 (2017) 65–68.
[15] N. Hua, W. Wang, Q. Wang, Y. Ye, S. Lin, L. Zhang, Q. Guo, J. Brechtl, P.K. Liaw, Mechanical, corrosion, and wear properties of biomedical Ti–Zr–Nb–Ta–Mo high entropy alloys, J. Alloy. Compd. 861 (2021) 157997.
[16] W.H. Liu, Z.P. Lu, J.Y. He, J.H. Luan, Z.J. Wang, B. Liu, Y. Liu, M.W. Chen, C.T. Liu, Ductile CoCrFeNiMox high entropy alloys strengthened by hard intermetallic phases, Acta Mater. 116 (2016) 332–342.
[17] N.H. Tariq, M. Naeem, B.A. Hasan, J.I. Akhter, M. Siddique, Effect of W and Zr on structural, thermal and magnetic properties of AlCoCrCuFeNi high entropy alloy, J. Alloy. Compd. 556 (2013) 79–85.
[18] Z.D. Han, H.W. Luan, X. Liu, N. Chen, X.Y. Li, Y. Shao, K.F. Yao, Microstructures and mechanical properties of Ti NbMoTaW refractory high-entropy alloys, Mater. Sci. Eng. A. 712 (2018) 380–385.
[19] Q. Li, H. Zhang, D. Li, Z. Chen, S. Huang, Z. Lu, H. Yan, WxNbMoTa refractory high-entropy alloys fabricated by laser cladding deposition, Materials 12 (2019) 533.
[20] S. Park, C. Park, Y. Na, H.-S. Kim, N. Kang, Effects of (W, Cr) carbide on grain refinement and mechanical properties for CoCrFeMnNi high entropy alloys, J. Alloy. Compd. 770 (2019) 222–228.
[21] T. Hori, T. Nagase, M. Todai, A. Matsugaki, T. Nakano, Development of non-equiatomic Ti-Nb-Ta-Zr-Mo high-entropy alloys for metallic biomaterials, Scr. Mater. 172 (2019) 83–87.
[22] S.-P. Wang, J. Xu, TiZrNbTa)-Mo high-entropy alloys: dependence of microstructure and mechanical properties on Mo concentration and modeling of solid solution strengthening, Intermetallics 95 (2018) 59–72.
[23] Z. Xiong, P. Tao, Z. Long, Z. Huang, K. Long, X. Zhu, X. Xu, H. Deng, H. Lin, W. Li, The effect of Ta addition on mechanical properties of Zr-based bulk metallic glasses, Intermetallics 153 (2023) 107779.
[24] C. Chen, Y. Chen, K.L. Li, S.Y. Yang, J. Wang, S. Wang, Y.R. Mao, L.M. Luo, Y. C. Wu, The ductile-brittle transition behaviors of W/Ta multilayer composites, J. Alloy. Compd. 946 (2023) 169377.
[25] B. Seo, H.-K. Park, C.-S. Park, K. Park, Role of Ta in improving corrosion resistance of titanium alloys under highly reducing condition, J. Mater. Res. Technol. 23 (2023) 4955–4964.
[26] J. Wu, X. Jiang, Y. Wang, J. Dong, L. Lou, Effects of Ta on microstructural stability and mechanical properties of hot corrosion resistant Ni-based single crystal superalloys during long-term thermal exposure, Mater. Sci. Eng. A. 806 (2021) 140829.
[27] C. Hu, Y.X. Xu, L. Chen, F. Pei, Y. Du, Mechanical properties, thermal stability and oxidation resistance of Ta-doped CrAlN coatings, Surf. Coat. Technol. 368 (2019) 25–32.
[28] X. Duan, Y. Huang, W. Liu, Q. Cai, W. Liu, Y. Ma, Effect of Ta on the microstructure and mechanical properties of W Ta alloys prepared by arc melting, Mater. Charact. 188 (2022) 111823.
[29] Z.D. Han, H.W. Luan, X. Liu, N. Chen, X.Y. Li, Y. Shao, K.F. Yao, Microstructures and mechanical properties of $Ti_x$NbMoTaW refractory high-entropy alloys, Mater. Sci. Eng. A. 712 (2018) 380–385.
[30] T. Nagase, M. Todai, T. Hori, T. Nakano, Microstructure of equiatomic and non-equiatomic Ti-Nb-Ta-Zr-Mo high-entropy alloys for metallic biomaterials, J. Alloy. Compd. 753 (2018) 412–421.
[31] J.A. Smeltzer, B.C. Hornbuckle, A.K. Giri, K.A. Darling, M.P. Harmer, H.M. Chan, C. J. Marvel, Nitrogen-induced hardening of refractory high entropy alloys containing laminar ordered phases, Acta Mater. 211 (2021) 116884.
[32] B. Wang, Q. Wang, N. Lu, X. Liang, B. Shen, Enhanced high-temperature strength of HfNbTaTiZrV refractory high-entropy alloy via Al2O3 reinforcement, J. Mater. Sci. Technol. 123 (2022) 191–200.
[33] D. Cui, Y. Zhang, L. Liu, Y. Li, L. Wang, Z. Wang, J. Li, J. Wang, F. He, Oxygen-assisted spinodal structure achieves 1.5 GPa yield strength in a ductile refractory high-entropy alloy, J. Mater. Sci. Technol. 157 (2023) 11–20.
[34] S.H. Chen, J.S. Zhang, S. Guan, T. Li, J.Q. Liu, F.F. Wu, Y.C. Wu, Microstructure and mechanical properties of WNbMoTaZrx (x = 0.1, 0.3, 0.5, 1.0) refractory high entropy alloys, Mater. Sci. Eng. A. 835 (2022) 142701.
[35] T. Xiang, P. Du, Z. Cai, K. Li, W. Bao, X. Yang, G. Xie, Phase-tunable equiatomic and non-equiatomic Ti-Zr-Nb-Ta high-entropy alloys with ultrahigh strength for metallic biomaterials, J. Mater. Sci. Technol. 117 (2022) 196–206.
[36] G. Chen, H. Yan, Z. Wang, K. Wang, N.I. Yves, Y. Tong, Effects of Mo content on the microstructure and mechanical properties of TiNbZrMox high-entropy alloys, J. Alloy. Compd. 930 (2023) 167373.
[37] Z. Zhang, M.M. Mao, J. Wang, B. Gludovatz, Z. Zhang, S.X. Mao, E.P. George, Q. Yu, R.O. Ritchie, Nanoscale origins of the damage tolerance of the high-entropy alloy CrMnFeCoNi, Nat. Commun. 6 (2015) 10143.
[38] X. Wen, Y. Wu, H. Huang, S. Jiang, H. Wang, X. Liu, Y. Zhang, X. Wang, Z. Lu, Effects of Nb on deformation-induced transformation and mechanical properties of HfNbxTa0.2TiZr high entropy alloys, Mater. Sci. Eng. A. 805 (2021) 140798.
[39] K.-K. Tseng, C.-C. Juan, S. Tso, H.-C. Chen, C.-W. Tsai, J.-W. Yeh, Effects of Mo, Nb, Ta, Ti, and Zr on Mechanical Properties of Equiatomic Hf-Mo-Nb-Ta-Ti-Zr Alloys, Entropy 21 (2018) 15.
[40] Y. Zhang, Y.J. Zhou, J.P. Lin, G.L. Chen, P.K. Liaw, Solid-Solution Phase Formation Rules for Multi-component Alloys, Adv. Eng. Mater. 10 (2008) 534–538.
[41] A. Takeuchi, A. Inoue, Classification of bulk metallic glasses by atomic size difference, heat of mixing and period of constituent elements and its application to characterization of the main alloying element, Mater. Trans. 46 (2005) 2817–2829.
[42] X. Yang, Y. Zhang, Prediction of high-entropy stabilized solid-solution in multi-component alloys, Mater. Chem. Phys. 132 (2012) 233–238.
[43] S. Guo, C.T. Liu, Phase stability in high entropy alloys: formation of solid-solution phase or amorphous phase, Prog. Nat. Sci. Mater. Int. 21 (2011) 433–446.
[44] S. Guo, C. Ng, J. Lu, C.T. Liu, Effect of valence electron concentration on stability of fcc or bcc phase in high entropy alloys, J. Appl. Phys. 109 (2011) 103505.
[45] S.-P. Wang, J. Xu, TiZrNbTaMo high-entropy alloy designed for orthopedic implants: As-cast microstructure and mechanical properties, Mater. Sci. Eng. C. 73 (2017) 80–89.
[46] S. Ge, H. Fu, L. Zhang, H. Mao, H. Li, A. Wang, W. Li, H. Zhang, Effects of Al addition on the microstructures and properties of MoNbTaTiV refractory high entropy alloy, Mater. Sci. Eng. A. 784 (2020) 139275.
[47] Z. An, S. Mao, T. Yang, C.T. Liu, B. Zhang, E. Ma, H. Zhou, Z. Zhang, L. Wang, X. Han, Spinodal-modulated solid solution delivers a strong and ductile refractory high-entropy alloy, Mater. Horiz. 8 (2021) 948–955.
[48] Y.D. Wu, Y.H. Cai, T. Wang, J.J. Si, J. Zhu, Y.D. Wang, X.D. Hui, A refractory Hf25Nb25Ti25Zr25 high-entropy alloy with excellent structural stability and tensile properties, Mater. Lett. 130 (2014) 277–280.
[49] C.R. LaRosa, M. Shih, C. Varvenne, M. Ghazisaeidi, Solid solution strengthening theories of high-entropy alloys, Mater. Charact. 151 (2019) 310–317.
[50] P. Thirathipviwat, S. Sato, G. Song, J. Bednarcik, K. Nielsch, J. Jung, J. Han, A role of atomic size misfit in lattice distortion and solid solution strengthening of TiNbHfTaZr high entropy alloy system, Scr. Mater. 210 (2022) 114470.
[51] I. Toda-Caraballo, P.E.J. Rivera-Díaz-del-Castillo, Modelling solid solution hardening in high entropy alloys, Acta Mater. 85 (2015) 14–23.
[52] C. Lee, G. Kim, Y. Chou, B.L. Musicó, M.C. Gao, K. An, G. Song, Y.-C. Chou, V. Keppens, W. Chen, P.K. Liaw, Temperature dependence of elastic and plastic deformation behavior of a refractory high-entropy alloy, Sci. Adv. 6 (2020) eaaz4748.

[53] B. Chen, S. Li, H. Zong, X. Ding, J. Sun, E. Ma, Unusual activated processes controlling dislocation motion in body-centered-cubic high-entropy alloys, Proc. Natl. Acad. Sci. 117 (2020) 16199–16206.
[54] F. Wang, G.H. Balbus, S. Xu, Y. Su, J. Shin, P.F. Rottmann, K.E. Knipling, J.-C. Stinville, L.H. Mills, O.N. Senkov, I.J. Beyerlein, T.M. Pollock, D.S. Gianola, Multiplicity of dislocation pathways in a refractory multiprincipal element alloy, Science 370 (2020) 95–101.
[55] E.P. George, W.A. Curtin, C.C. Tasan, High entropy alloys: a focused review of mechanical properties and deformation mechanisms, Acta Mater. 188 (2020) 435–474.
[56] O.N. Senkov, J.M. Scott, S.V. Senkova, D.B. Miracle, C.F. Woodward, Microstructure and room temperature properties of a high-entropy TaNbHfZrTi alloy, J. Alloy. Compd. 509 (2011) 6043–6048.